Journal of Luminescence 196 (2018) 337–346

Contents lists available at ScienceDirect

Journal of Luminescence

journal homepage: www.elsevier.com/locate/jlumin

Reassignment of electronic transitions in the laser-activated spectrum of nanocrystalline Y_2O_3:Er^{3+}

D. den Engelsen, G.R. Fern, T.G. Ireland*, J. Silver

Centre for Phosphor and Display Materials, Wolfson Centre for Materials Processing, Brunel University London, Uxbridge, Middlesex UB8 3PH, UK

ARTICLE INFO

Keywords:
Assignment
Temperature behaviour
Cross-relaxation
Hot band
Laser energy
Line width

ABSTRACT

The laser-activated spectra of nanocrystalline Y_2O_3:Er^{3+} recorded at various temperatures and two excitation energies are described and analysed herein. Based on recently published modified values of the C_2-type Stark splitting of Er^{3+} in the cubic Y_2O_3 lattice, the Er^{3+} multiplets in the observed spectra have been re-assigned. The upconversion routes of three $^2H_{11/2} \rightarrow {}^4I_{15/2}$ hot bands from $^4S_{3/2}$ Kramers doublets have been traced, based on an Arrhenius-type analysis of these hot bands. We observed 5 peaks in the $^2H_{11/2} \rightarrow {}^4I_{15/2}$ hot band region with a different temperature behaviour. These bands belong to the $^2P_{3/2} \rightarrow {}^4I_{9/2}$ multiplet and their deviating temperature behaviour has been explained in terms of a cross relaxation mechanism. From the ratio between the laser-activated spectra that were recorded at different excitation energies we concluded that the two-photon absorption process becomes more efficient upon increasing the excitation energy. We have also put forward an explanation for the gradual broadening of the fluorescence bands of the $^2H_{11/2} \rightarrow {}^4I_{15/2}$ multiplet in going from 518 nm to 542 nm. The higher Stark splitting levels are due to a stronger electrostatic field of the host lattice and experience therefore a higher electron-phonon interaction, which explains the observed increase of FWHM at larger wavelengths.

1. Introduction

Nanoscience and nanotechnology have come a long way since we published our first paper on the effect of particle morphology and crystallite size on the upconversion luminescence from sub-micron particles containing nanocrystals of Er^{3+},Yb^{3+} doped Y_2O_3 [1]. The drivers for the continual interest are both fundamental understanding of nanoparticle properties and technological interests, which endeavour to develop nano-materials for a wide range of applications. The possibility to design and synthesise new or modified materials at the near atomic level that yield both chemical and physical properties that are dependent on particle size has already seen large scale commercial applications in displays and lighting applications using for example quantum dot phosphors [2]. It was pointed out in as early as 2004 that rare-earth-element doped nanoparticles were promising up-converting fluorescence labels in the detection of biological interactions [3]. In fact, rare-earth-element doped nanoparticles may have widespread use as novel luminescent probes for numerous applications in nanobiophotonics. However even though some are remarkably photostable, have narrowband photoluminescence, have efficient anti-Stokes emission and long luminescence lifetimes, all properties necessary for such applications, there was and still is much concern about their toxicity in both in vivo and in vitro applications [4]. Both upconverting rare-earth-element doped nanoparticles and quantum dots have been considered for use as in vivo near-infrared fluorescence imaging of cancer [5]. Both the properties and applications of upconversion nanoparticles including their use in biology and diagnostics have also recently been reviewed [6,7]. It is apparent that from all the work since our studies that further applications of the upconverting nanoparticles will come with increased understanding of their upconverting properties.

The articles we published in 2001 focussed on the laser-activated (LA) spectra of Y_2O_3:Er^{3+} in the visible and near IR region [1,8]. A He-Ne laser was used for excitation. The motive for the work was to better understand the upconversion behaviour of the Er^{3+} ion in the Y_2O_3 host lattice, when the materials were nanocrystalline. In the first study [1], in which we focussed on the $^2H_{11/2} \rightarrow {}^4I_{15/2}$ multiplet, we observed two types of hot bands, which were attributed to the presence of Er^{3+} ions at two different lattice sites in cubic Y_2O_3, namely the C_2 and C_{3i} sites. In this article we shall use the following definition of hot band: a cluster of spectral transitions belonging to a multiplet that largely disappears upon decreasing the temperature from ambient conditions to liquid nitrogen temperature, while upon increasing the temperature a moderate increase in intensity is observed before thermal quenching sets in.

Our assignment of the $^2H_{11/2} \rightarrow {}^4I_{15/2}$ hot bands in 2001, which was

* Corresponding author.
E-mail address: terry.ireland@brunel.ac.uk (T.G. Ireland).

https://doi.org/10.1016/j.jlumin.2017.12.053
Received 5 November 2017; Received in revised form 24 December 2017; Accepted 26 December 2017
Available online 27 December 2017

largely based on the different temperature behaviour of the relevant spectral transitions between 519 nm and 540 nm, was criticized by Tanner et al. [9]. In an earlier paper Tanner and Wong [10] described a part of the LA-spectrum (activated by a 488 nm Ar^+ laser) of Y_2O_3:Er^{3+} and calculated the temperature in the nanocrystals from the spectra upon laser excitation. These publications were one motive to reconsider the assignment of transitions in the spectrum of Y_2O_3:Er^{3+}.

Another motive was to study the evaluation method of the activation energy of the $^2H_{11/2} \rightarrow {}^4I_{15/2}$ hot band. Based on a simple three-level system referring to the $^2H_{11/2}$ (level 3), $^4S_{3/2}$ (level 2), and $^4I_{15/2}$ (ground level) levels, Shinn et al. [11] proposed that the activation energy ΔE_{23} for the $^2H_{11/2} \rightarrow {}^4I_{15/2}$ hot band may be calculated from:

$$\frac{R_2}{R_3} = Pe^{-\Delta E_{23}/kT} \quad (1)$$

where R_2 and R_3 are the radiances (integrated intensities) of the $^4S_{3/2} \rightarrow {}^4I_{15/2}$ and $^2H_{11/2} \rightarrow {}^4I_{15/2}$ transitions respectively, the pre-exponential factor P contains among others the degeneracies of the levels 2 and 3, k is Boltzmann's constant and T is the absolute temperature. The advantage of using Eq. (1) is that the ratio R_2/R_3 does not depend on the excitation location of the sample. Shinn et al. showed that this equation may be used in the case of a non-crystalline sample, which did not show Stark splitting of the electronic levels [11]. In the case of Y_2O_3 doped with Er^{3+} the Stark splitting of the electronic levels render the definition of ΔE_{23} less clear; moreover, the temperature behaviour of Stark components in a multiplet is not necessarily uniform, which may lead to contradictory results for the activation energy.

Thanks to the works of Gruber [12–15], which started in the nineteen sixties and continued until 2010, the energy levels and crystal field splitting of electronic levels of Er^{3+} at C_2 and C_{3i} sites in Y_2O_3 have been calculated and are now available from the IR- to the UV-energy range. Apart from the magnetic-dipole transitions in the IR between the first excited manifold, $^4I_{13/2}$, and the ground-state manifold, $^4I_{15/2}$, no magnetic-dipole transitions have been identified for Er^{3+} in C_{3i} sites in the other spectral regions [12,13,15].

The above considerations prompted us to revisit the LA-spectra of Y_2O_3:Er^{3+} and to investigate the temperature behaviour over a larger temperature range, namely from −190 °C to 250 °C, than in our previous studies. This enlarged temperature range provides more experimental evidence to distinguish between thermal quenching and hot band behaviour as represented in Eq. (1). Thermal quenching of the luminescence from rare-earth-doped crystals can be described by a single barrier model in terms of the Fermi-Dirac equation [16,17] and is usually observed at temperatures > 25 °C. For our analyses of the temperature behaviour of the spectral transitions we shall combine the single barrier model of thermal quenching with a hot band description similar to Eq. [1].

As we have extensively reported the Raman bands of the Y_2O_3 lattice in our earlier work [1], these will not be referred to in the current work.

2. Experimental and methods

2.1. Synthesis

The following chemicals were used in the synthesis of the nanocrystalline spherical Y_2O_3:Er^{3+} phosphor particles: yttrium oxide and erbium oxide (Neomaterials, UK, 99.99%), nitric acid (Fisher Scientific, UK, PrimarPlus, S.G. 1.42, < 68%) and urea, (Sigma Aldrich, UK). All chemicals were used without additional purification. Y_2O_3 phosphor doped with 1 mol% Er^{3+} was prepared by the urea hydrothermal precipitation method [18,19] followed by annealing at 1020 °C in air.

2.2. X-ray powder diffraction

The crystallinity of the cubic Y_2O_3:Er^{3+} particles was checked by X-ray powder diffraction using a Bruker D8 Advance X-ray diffractometer (XRD) fitted with a nickel-filtered copper source, CuKα at λ = 1.5406 Å, and a LynxEye™ silicon strip detector.

2.3. Micro-Raman and laser-induced fluorescence spectra

Laser-induced fluorescence spectra of the samples were measured with a Horiba Jobin Yvon Labram HR monochromator by excitation with a He-Ne laser at temperatures varying between −190 °C and +250 °C in steps of 25 °C or sometimes 50 °C. The wavelength error of the Labram monochromator was smaller than ± 0.02 nm. Transmission filters (10% and 25%) were used to vary the excitation power (0.8 mW and 2 mW) of the He-Ne laser. Upon stepping from one temperature to another the effects of temperature drift had to be nullified. This was done by monitoring the position of the laser spot on the sample by a microscope and careful manual readjustment using the automated microscope stage of prominent surface features as a marker. The spectra were recorded over the temperature range −190 °C to 250 °C in steps of 25 °C or 50 °C using a THMS600 heating and cooling stage, which is controlled by a TMS94 temperature controller with a temperature accuracy of +/−0.1 °C.

2.4. Transmission electron microscopy

For the studies in the transmission electron microscope (TEM) copper grids coated with thin carbon films having small holes (holey carbon films) were used as substrates: these are transparent to the high-energy electrons. The TEM work was done on a JEOL 2100F (Japan).

2.5. Evaluation methods

Before presenting the results of our analyses, the methods used in analysing the spectra will be explained in this section. Two methods were used, the first is a deconvolution technique to accurately determine the spectral radiance at the peak of an emission band and the integrated intensity (radiance) of that emission band; the second is a method to evaluate the thermal quenching barrier and hot band activation energy from the temperature behaviour of an individual spectral transition.

2.5.1. Deconvolution

The fluorescence bands, also indicated by transitions, lines and peaks, in the LA-spectra of Y_2O_3:Er^{3+} are rather narrow and can be well represented by Lorentzian profiles. The spectral radiance $SR_i(\lambda)$, where λ represents the wavelength, can be written as:

$$SR_i(\lambda) = \sum_i \frac{A_i}{1 + \frac{(\lambda - \lambda_i)^2}{s_i^2}} \quad (2)$$

where A_i is the maximum spectral radiance of the ith peak, λ_i is the wavelength at the maximum intensity of i, s_i is the half width at half maximum of peak i. The radiance R_i of the ith transition can be written as:

$$R_i = \int_{-\infty}^{\infty} \frac{A_i d\lambda}{1 + \frac{(\lambda - \lambda_i)^2}{s_i^2}} = A_i s_i \pi \quad (3)$$

The radiance R_i of the transitions is used to calculate the activation energy of the transition and to characterize the nature of the temperature dependence, to be discussed hereafter. Fig. 1 shows an example of a deconvolution with a skew background.

2.5.2. Temperature behaviour

The temperature behaviour of the fluorescence bands in the rich LA-spectrum of Y_2O_3:Er^{3+} is one of the most intriguing features. We found that the temperature behaviour of the spectral transitions of Y_2O_3:Er^{3+}

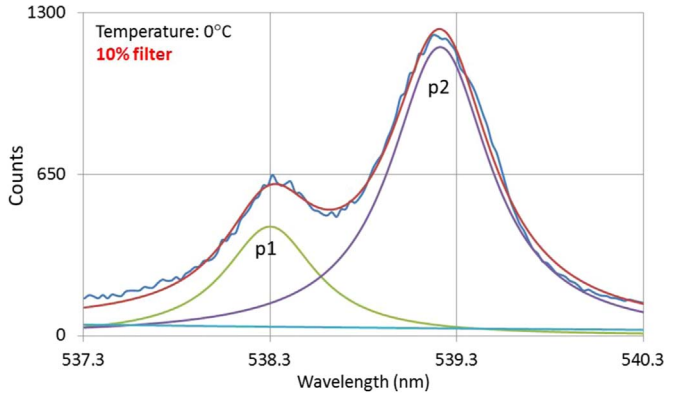

Fig. 1. Deconvolution of the 539 nm doublet in the $^2H_{11/2} \rightarrow {}^4I_{15/2}$ hot band region of $Y_2O_3:Er^{3+}$. A least-squares fit was carried out using Microsoft's Excel Solver. FWHM of p1 is 0.595 nm, FWHM of p2 is 0.650 nm.

can be distinguished in 5 categories or types, indicated in Figs. 2 and 3. Fig. 2 presents 4 of the 5 types of temperature behaviour as spectra, while Fig. 3 shows the radiance (integrated luminescence intensity) of the 5 types in an Arrhenius-type plot. The characteristics of the four types introduced in Fig. 2 are more clearly illustrated in the Arrhenius-type plot of Fig. 3.

Type 1a is the most prevailing temperature behaviour in the LA-spectra of $Y_2O_3:Er^{3+}$, characteristic for the strong fluorescence bands. The general features are: a monotonic decrease of the radiance (integrated intensity) upon increasing the temperature and two slopes in the Arrhenius plot: a rather slow decrease of the radiance upon increasing the temperature at low temperatures and a fast decrease in radiance at temperatures > 50 °C.

Type 2a is the hot band behaviour of the $^2H_{11/2} \rightarrow {}^4I_{15/2}$ bands. The increase of the radiance at low temperatures is almost 3 decades before it levels off at temperatures > 75 °C.

Type 1c has hot-band characteristics, but the activation energy at low temperatures is much smaller than for type 2a. Type 1b does not show a variation of the radiance at low temperatures, at high temperatures it gets quenched as well.

Type 2b shows the most enigmatic behaviour. At very low temperatures it has the characteristics of type 1a and upon increasing the temperature from −50 °C to 250 °C it gets the characteristics of type 2a. This can also be noticed in Fig. 4, in which we have plotted the FWHMs of the various temperature types shown in Fig. 3.

The FWHMs represented in Fig. 4 are two times the s-values (defined in Eqs. (2) and (3)) as determined from the deconvolution from the various bands. The types represented in Fig. 4a show a regular behaviour, in which the FWHM increases monotonically (almost parabolic) with temperature. Type 2b in Fig. 4b illustrates a completely different characteristic: at T = 223 K (−50 °C) a different process takes over. This behaviour will be explained in the discussion section.

2.5.3. Combination of thermal quenching and hot band behaviour

We shall now introduce an equation that describes the thermal quenching at high temperatures (~ > 50 °C) and the hot band disappearance at low temperatures (~ < 50 °C).

This equation can be written as:

$$R(T) = \frac{Ce^{-E_u/kT}}{1 + Be^{-E_q/kT}} \tag{4}$$

where R(T) is the radiance (area under the spectral curve) for an individual spectral transition as calculated with Eq. (3) from deconvoluted bands, C is a pre-exponential factor, E_u is the upconversion energy of the hot hand, represented as ΔE_{23} in Eq. (1), B is the frequency factor describing thermal quenching in a single barrier model [16,17] and E_q is the quenching energy. C, E_u, B and E_q were fitted to the experimental

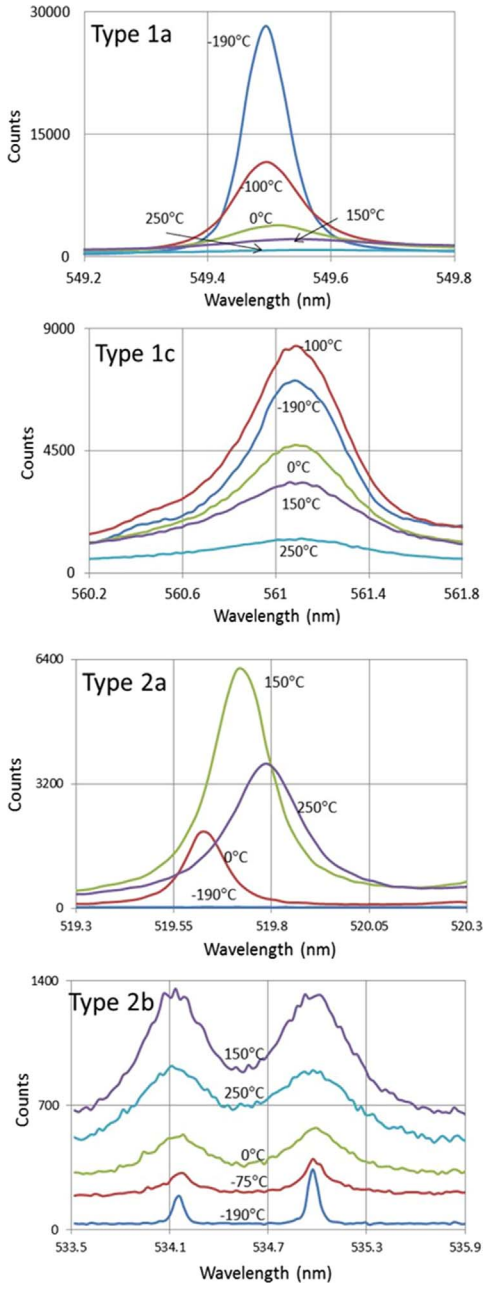

Fig. 2. Four categories of temperature behaviour in the LA-spectrum of $Y_2O_3:Er^{3+}$ are presented. Only five or four different temperatures are shown for reasons of clarity. Type 1a: valid for strong fluorescence bands. Type 1c: quasi-hot band behaviour, usually weak bands. Type 2a: hot band behaviour for $^2H_{11/2} \rightarrow {}^4I_{15/2}$ bands. Type 2b: mixed behaviour.

data points with a least squares algorithm. Instead of minimizing:

$$\sum_{T_i} [R(T_i)_{\exp} - R(T_i)_{fit}]^2 \tag{5}$$

we minimized the sum of normalized squares:

$$\sum_{T_i} \left[\frac{R(T_i)_{\exp} - R(T_i)_{fit}}{R(T_i)_{\exp}} \right]^2 \tag{6}$$

In this way it is possible to fit a curve that covers a range of more than three decades as shown in Fig. 3.

The numerator in Eq. (4) is the Boltzmann factor indicating the hot band behaviour: the increase of the radiance when the temperature is increased in the low temperature region (> 50 °C). The denominator describes the quenching of the luminescence at high temperature. For

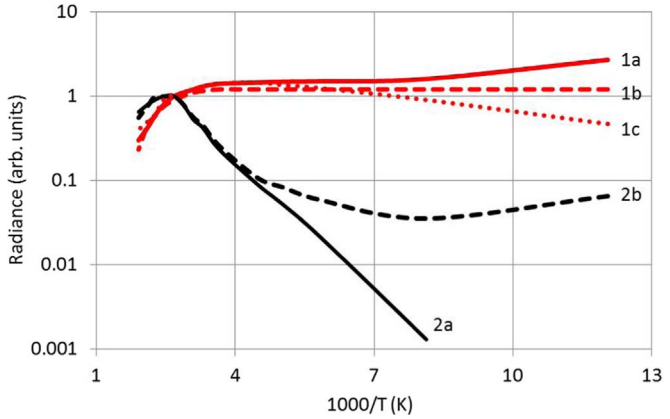

Fig. 3. Arrhenius plot of the radiance of fluorescence bands in Y_2O_3:Er^{3+}. Type 1b (not shown in Fig. 1) illustrates the gradual transition from 1a to 1c.

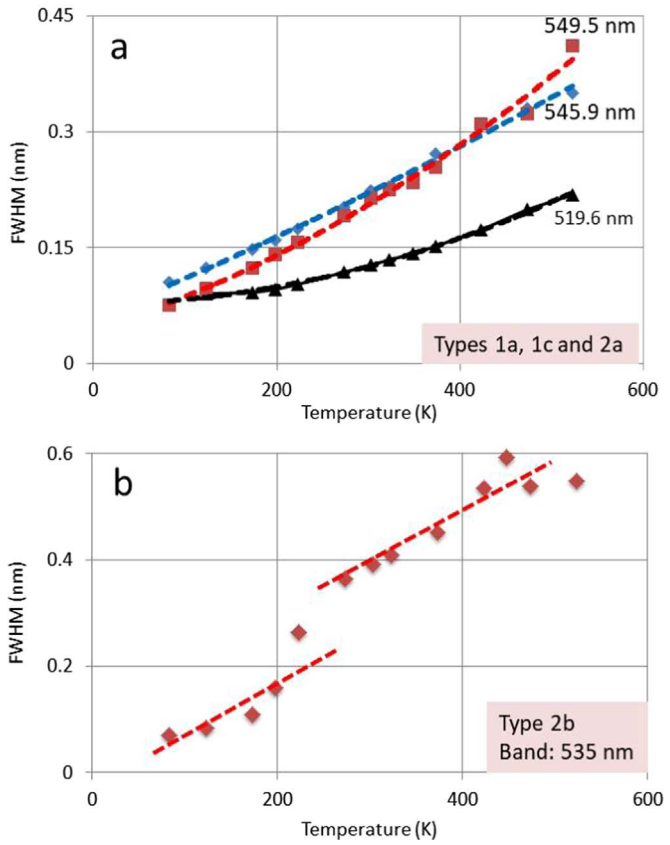

Fig. 4. FWHM of as a function of temperature. a: types 1a, 1c and 2a. b: type 2b.

type 1b Eq. (4) becomes the Fermi-Dirac equation, because $E_u = 0$, while for type 1a E_u is negative (i.e.: the exponent in the Eq. (4) is positive). For type 2a and 2b behaviour we don't have sufficient data to fit E_q (and B).

This calculation method refers to an individual spectral transition only and is not dependent on the behaviour of other bands. In stepping from one temperature to another it is required that exactly the same location of the sample is excited: in this way it is possible to make reliable Arrhenius plots of individual transitions.

3. Results

3.1. STEM images

Fig. 5 presents scanning transmission electron microscope (STEM) images of the spherical Y_2O_3:Er^{3+} particles. Fig. 5b is the panchromatic image of the STEM-image shown in Fig. 5a. From these images it can be concluded that the average diameter of the spherical particles is ~ 250 nm and that these particles contained crystallites of ~ 30 nm. This was concluded from TEM analyses, not shown.

3.2. LA-spectra

Figs. 6 and 7 show LA-spectra of Y_2O_3:Er^{3+}. Fig. 6 is an overview, illustrating the strongest fluorescence bands at three different temperatures. It should be stressed that spectra recorded at different temperatures in one figure refer to the same position on the sample as mentioned above.

The overall appearance of the LA-spectra of Y_2O_3:Er^{3+} deviates considerably from the appearance of the photoluminescence (PL) spectra of this material; see for instance Gruzintsev et al. [20]. In the PL spectra the $^4S_{3/2} \rightarrow {}^4I_{15/2}$ multiplet ($540 < \lambda < 565$ nm) yields the strongest fluorescence bands, whereas the LA-spectra yield the strongest emission bands in the $^4F_{9/2} \rightarrow {}^4I_{15/2}$ multiplet ($645 < \lambda < 685$ nm). This difference is caused by the excitation process. The Stokes bands in the LA-spectrum at $\lambda > 632.8$ nm are strong, because these are generated by a one-photon absorption process. The anti-Stokes bands at $\lambda < 632.8$ nm are based on a two-photo absorption process, which is less efficient. We have identified two very weak bands that are generated by a three-photon absorption process. This doublet is indicated by an arrow in the −190 °C spectrum that is presented in Fig. 7a. The doublet is at 419.0 nm and 420.4 nm and is ascribed to the $^2H_{9/2} \rightarrow {}^4I_{9/2}$ multiplet. The $^2H_{9/2}$ electronic level of Er^{3+} in the Y_2O_3 lattice is positioned at 36,400 cm^{-1} (centroid frequency) by Gruber et al. [15] and requires three He-Ne photons to be populated. All observed multiplets in the LA-spectra have been identified and are summarized in Table 1.

The $^2H_{11/2} \rightarrow {}^4I_{15/2}$ hot bands are presented in Fig. 8 at −150 °C, −100 °C, −50 °C, 0 °C and +30 °C. For reasons of clarity only a limited number of spectra are presented in this Figure. Apart from the hot-band character, Fig. 8 shows another interesting phenomenon, viz. the gradual broadening of the fluorescence bands in going from 518 nm to 542 nm. This phenomenon can also be observed in the $^4S_{3/2} \rightarrow {}^4I_{15/2}$ and $^4F_{9/2} \rightarrow {}^4I_{15/2}$ multiplets. It was previously reported by Kisliuk et al. in 1964 [12] and up to now there does not seem to be an adequate explanation. As preliminary explanation for this effect we suggest that the higher Stark levels are due to a stronger electrostatic field of the host lattice and experience therefore a higher electron-phonon interaction, which explains the observed increase of FWHM at larger wavelengths.

In Fig. 9 the deviating behaviour of the bands at 527.0 nm, 530.2 nm, 532.3 nm, 534.2 nm and 535 nm is shown. Since the fluorescence bands in the spectrum recorded at −190 °C in Fig. 9 are not vanishing, they apparently belong to another spectral transition that is not a hot band. In 2001 we suggested that these bands could be assigned to $^2H_{11/2} \rightarrow {}^4I_{15/2}$ C_{3i} transitions. As indicated by Gruber et al. [14,15], this is not very likely. Tanner suggested that these transitions could be assigned to $^2P_{3/2} \rightarrow {}^4I_{9/2}$ C_2 transitions [9]. In Table 2 the correspondence between the observed transition frequencies and the calculated frequencies, using Gruber's et al. [15] data, is shown. From Table 2 it can be concluded that the fluorescence bands at −190 °C in Fig. 9 can indeed be assigned to $^2P_{3/2} \rightarrow {}^4I_{9/2}$ C_2 transitions of Er^{3+} in cubic Y_2O_3. This assignment by itself does not explain their odd temperature behaviour (type 2b); we shall consider this behaviour in more detail in the Section 4.

The electronic level $^2P_{3/2}$ of Er^{3+} is important in the LA-spectra of

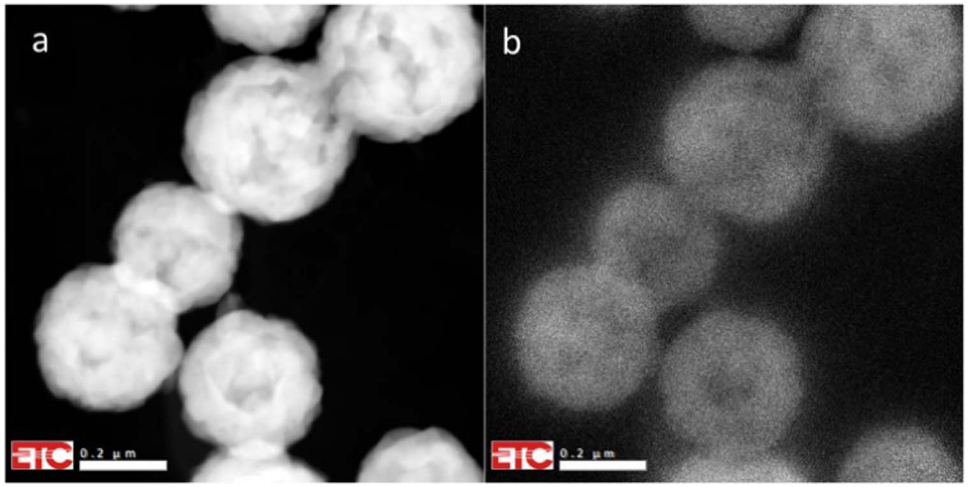

Fig. 5. STEM images of $Y_2O_3:Er^{3+}$ (1%). (a) High angle annular dark-field (HAADF) image. (b) Panchromatic image of same area as shown in (a).

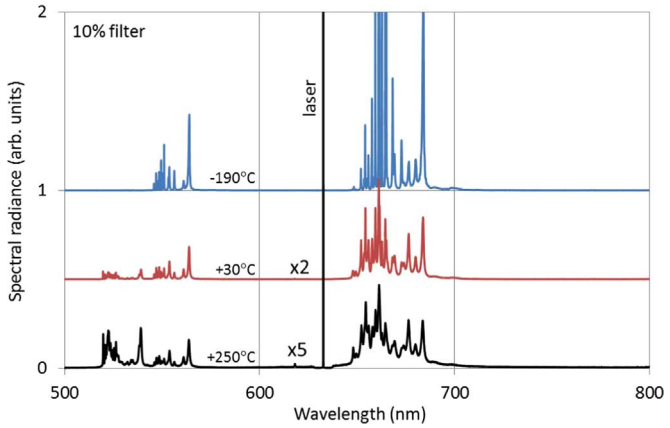

Fig. 6. Strong fluorescence bands in LA-spectra of $Y_2O_3:Er^{3+}$ (1%).

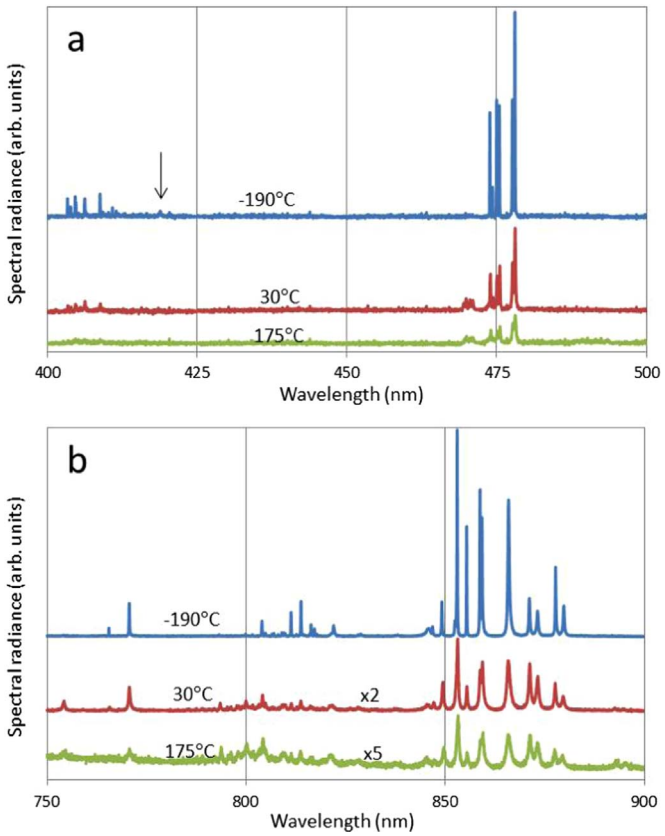

Fig. 7. Weak(er) fluorescence bands. (a) Wavelengths from 400 nm to 500 nm. (b) Wavelengths from 750 nm to 900 nm. In this figure the LA- spectra at +175 °C are represented, because the fluorescence at 250 °C has almost been quenched.

$Y_2O_3:Er^{3+}$, because the two Stark sub-levels of this electronic level (at 31,488 cm^{-1} and 31,299 cm^{-1}) are only slightly lower than the two-photon excitation of the He-Ne laser at 31,606 cm^{-1}. So, this level will initially be populated upon He-Ne irradiation and two-photon absorption. De-excitation of the $^2P_{3/2}$ levels occurs through radiationless energy transfer, as indicated by Silver et al. [1]. In allowing also de-excitation of the $^2P_{3/2}$ levels by direct radiation and using Gruber's et al. [15] data of the electronic levels, we can assign all observed multiplets in the LA-spectrum of $Y_2O_3:Er^{3+}$. This assignment is summarized in Table 1.

The transitions from the $^4F_{9/2}$, $^4S_{3/2}$ and $^2H_{11/2}$ levels to the ground level, $^4I_{15/2}$, are relatively strong. The transitions from $^2P_{3/2}$ and $^2K_{15/2}$ to non-ground levels are at least an order of magnitude weaker.

The assignment presented in Table 2 deviates considerably from the assignment published previously [1]. The reason is that the new data of Gruber et al. [15] were not available in 2001, while the position of the $^2H_{9/2}$ level of Er^{3+} in Dieke's diagram [12,21] at 24,750 cm^{-1} has been positioned at 36,410 cm^{-1} according to Gruber's et al. recent re-assignment [15]. They based their reassignments on more sophisticated techniques in analysing the weak, broad unresolved absorption spectra of overlapping manifolds in the blue and near UV.

We have checked all recorded bands in the LA-spectrum of $Y_2O_3:Er^{3+}$ with the C_2-type transitions that can be calculated from Gruber's data. The agreement is excellent: the maximum deviation is 6 cm^{-1}. An example of this assignment is shown in Table 3 for the $^4S_{3/2} \rightarrow {}^4I_{13/2}$ and $^2P_{3/2} \rightarrow {}^4S_{3/2}$ multiplets. In this Table we have also indicated the temperature behaviour of the individual transitions and the M_J quantum number of the upper Kramers doublet that is involved in the transition. We shall come back to this distinction in the discussion section.

Albeit the agreement between the experimental and calculated (from Gruber's data) transition frequencies is satisfactory, we found 6 bands in the LA-spectrum of $Y_2O_3:Er^{3+}$ that could not be assigned. These bands are presented in Table 4. Not-assigned means that there is no agreement (< 10 cm^{-1}) with any transition calculated from Table 1 of Gruber et al. [15].

It should be mentioned that the 519.6 nm peak in the $^2H_{11/2} \rightarrow {}^4I_{15/2}$ multiplet cannot be assigned by applying Gruber's data. This peak is the most left transition in Fig. 8. By assuming that the value of level 39 in columns 8 and 9 in Gruber's et al. Table 1 be 19,244 cm^{-1} instead of 19,218 cm^{-1} [15], the bands at 519.6 nm and 522.0 nm can be

Table 1
Assignment of the LA-spectrum of $Y_2O_3:Er^{3+}$.

Transition	Median/centroid		
	Observed nm	Observed cm^{-1}	Gruber[a] cm^{-1}
$^4S_{3/2} \rightarrow {}^4I_{13/2}$	863	11,587	11,590
$^2P_{3/2} \rightarrow {}^4S_{3/2}$	762	13,123	13,120
$^4F_{9/2} \rightarrow {}^4I_{15/2}$	664	15,060	15,062
$^2P_{3/2} \rightarrow {}^4F_{9/2}$	620	16,129	16,120
$^4S_{3/2} \rightarrow {}^4I_{15/2}$	553	18,083	18,171
$^2P_{3/2} \rightarrow {}^4I_{9/2}$	530	18,860	18,890
$^2H_{11/2} \rightarrow {}^4I_{15/2}$	529	18,904	18,901
$^2K_{15/2} \rightarrow {}^4I_{13/2}$	479	20,877	20,870
$^2P_{3/2} \rightarrow {}^4I_{11/2}$	472	21,186	21,110
$^2H_{9/2} \rightarrow {}^4I_{9/2}$	419.5	23,840	23,850
$^2G_{9/2} \rightarrow {}^4I_{15/2}$	409	24,450	24,400
$^2P_{3/2} \rightarrow {}^4I_{13/2}$	405	24,690	24,710

[a] Centroid frequency calculated from Gruber's data [13,15].

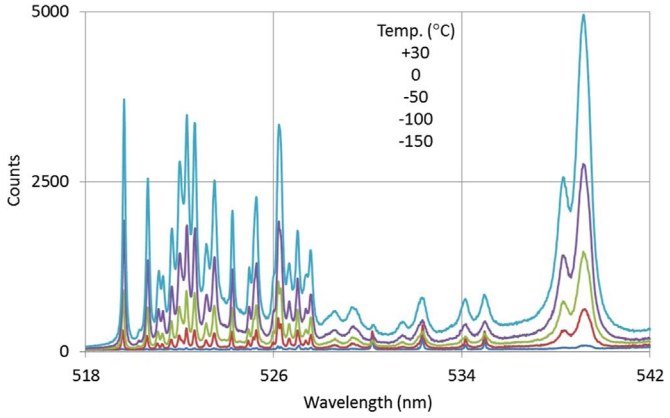

Fig. 8. Hot band region of $Y_2O_3:Er^{3+}$. Spectra recorded at −150 °C, −100 °C, −50 °C, 0 °C and +30 °C are shown.

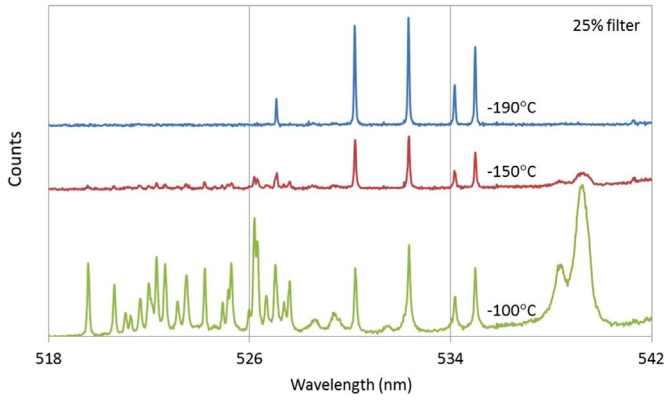

Fig. 9. The bands at 527.0 nm, 530.2 nm, 532.3 nm, 534.2 nm and 535 nm do not vanish at −190 °C.

Table 2
$^2P_{3/2} \rightarrow {}^4I_{9/2}$ C_2 transitions.

LA-spectrum		Ref. [8]
nm	cm^{-1}	cm^{-1}
527.06	18,973	18,975
530.17	18,862	18,863
532.32	18,786	18,787
534.16	18,721	18,723
534.97	18,693	18,695

Table 3
$^4S_{3/2} \rightarrow {}^4I_{13/2}$ and $^2P_{3/2} \rightarrow {}^4S_{3/2}$ transitions.

Transition	Experimental		Gruber[a]		
	nm	cm^{-1}	cm^{-1}	TB[b]	M_J exc.[c]
$^2P_{3/2} \rightarrow {}^4S_{3/2}$	754.3	13,257	13,257	1b	3/2
	765.6	13,062	13,068	1a	1/2
	770.6	12,977	12,981	1a	1/2
$^4S_{3/2} \rightarrow {}^4I_{13/2}$	849.2	11,776	11,776	1b/1c	3/2
	853.1	11,723	11,721	1a	1/2
	855.4	11,690	11,689	1a	1/2
	858.8	11,644	11,643	1a	1/2
	866.0	11,547	11,547	1a	1/2
	871.1	11,480	11,478	1b/1c	3/2
	873.2	11,452	11,451	1b/1c	3/2
	877.7	11,393	11,391	1a	1/2
	879.8	11,366	11,364	1a	1/2

[a] Calculated from Gruber's data [15].
[b] Temperature behaviour as defined in Figs. 2 and 3.
[c] M_J quantum number of the excited electronic level involved in the transition.

Table 4
Not identified transitions in LA-spectrum of $Y_2O_3:Er^{3+}$.

nm	cm^{-1}	Multiplet[a]
652.1	15,335	$^4F_{9/2} \rightarrow {}^4I_{15/2}$
523.5	19,103	$^2H_{11/2} \rightarrow {}^4I_{15/2}$
521.1	19,190	
470.0	21,279	$^2P_{3/2} \rightarrow {}^4I_{11/2}$
470.6	21,250	
405.3	24,675	$^2P_{3/2} \rightarrow {}^4I_{13/2}$

[a] Multiplet to which the band(s) could belong.

assigned to the $^2H_{11/2} \rightarrow {}^4I_{15/2}$ multiplet. Apart from the good level matching, another argument in favour of this correction is that these two bands also have the type 2a temperature behaviour as the other bands in this multiplet.

It is tempting to assume that the non-identified bands in Table 4 are C_{3i}-type transitions. This cannot be concluded from the recorded LA-spectra and we leave this question open for future investigations.

3.3. Temperature behaviour

Fig. 10 is an Arrhenius plot, showing the temperature behaviour of two bands of the $^4S_{3/2} \rightarrow {}^4I_{15/2}$ multiplet, viz. the peaks at 545.9 nm and 549.5 nm. In Fig. 10 we have plotted the radiance along the

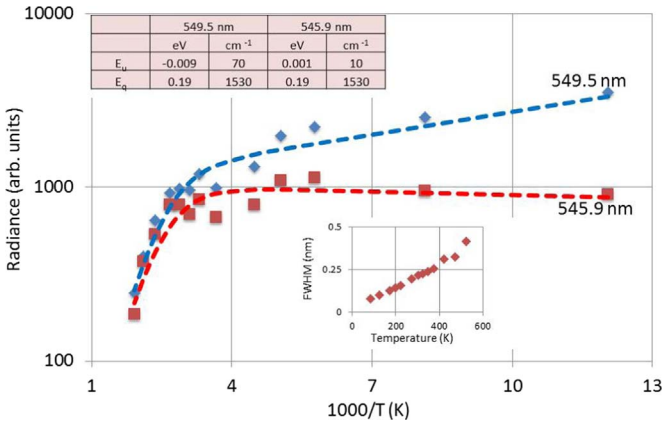

Fig. 10. Arrhenius plot of the radiances of the 545.9 nm and 549.5 nm bands of $Y_2O_3:Er^{3+}$; the laser was attenuated with a 25% transmission filter. The dashed curves, described by Eq. (4), have been fitted to the experimental points. The insert is a plot of the FWHM for the 549.5 nm transition versus temperature (in K).

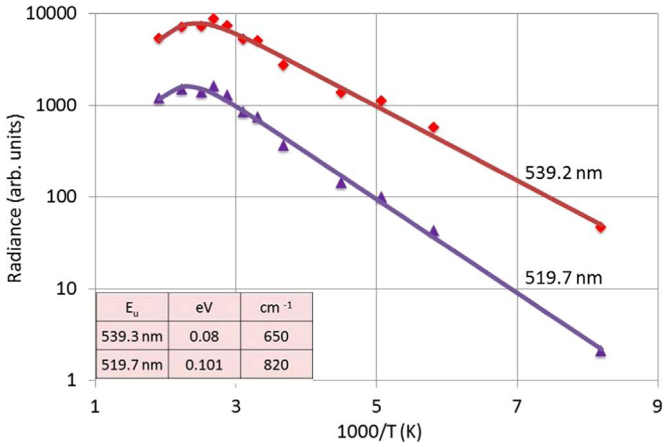

Fig. 11. Arrhenius plot of the radiances of the 539.2 nm and 519.7 nm bands of $Y_2O_3:Er^{3+}$, excited using a 25% transmission filter. The full curves are according to Eq. (4), fitted to the experimental points.

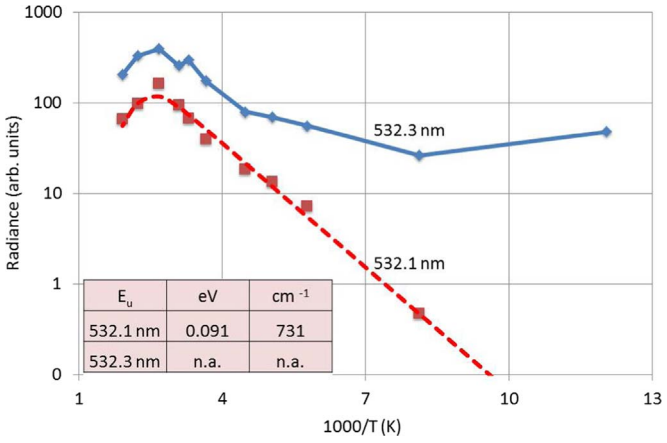

Fig. 12. Arrhenius plot of the radiances of the 532.3 nm and 532.1 nm bands of $Y_2O_3:Er^{3+}$. The dashed curve for 532.1 nm is according to Eq. (4), fitted to the experimental points. Fitting for type 2b behaviour of band 532.3 nm was impossible.

ordinate. As mentioned in the previous section, the experimental points are integrated intensities, calculated with Eq. (4) from the deconvoluted Lorentzian profiles. The radiance differs clearly from the spectral radiance at maximum, as can be seen in Fig. 1: type 1a refers to the behaviour of the 549.5 nm band. Radiance is the correct criterion to calculate activation energies, since it has the dimension of W sr^{-1} m^{-2}. The insert of Fig. 10 shows that the FWHM increases by almost a factor of 4 upon increasing the temperature from −190 °C (83 K) to +250 °C (523 K). This factor induces an error of about 25% in the activation energy if it would be based upon spectral radiance instead of radiance.

The upconversion energy E_u for the 549.5 nm band is negative: in fact, this energy is a down conversion energy as we shall argue in the discussion section. The value of E_u for the 545.9 nm is very small and, in view of the spread of the experimental data points, it may be set to 0. The temperature behaviour of this band is type 1b.

Fig. 11 is an Arrhenius plot of the radiances of the two extreme hot bands of the $^2H_{11/2} \rightarrow {}^4I_{15/2}$ multiplet, viz. the 539.2 nm and 519.7 nm bands. The two bands in Fig. 11 represent the typical type 2a character. We selected these bands for the determination of the activation energy, because these are rather strong and do not suffer from too much overlap: this makes the deconvolution more reliable. The values for E_u of these two bands differ significantly from each other, which is not surprising because the upconversion from $^4S_{3/2}$ to $^2I_{11/2}$ may refer to different sub-levels. From the E_u values we can try to identify which energy level of the $^4S_{3/2}$ doublet is involved in the upconversion. This is indicated in Table 5.

From Table 5 it can be concluded that the upconversion from the $^4S_{3/2}$ multiplet to the 519.7 nm and 539.3 nm bands is from the same level (level 33 in Gruber's Table [15]). The agreement between the calculated $^4S_{3/2}$ levels and Gruber's data is not perfect; nevertheless, from this calculation we may exclude level 32 in Gruber´s Table as the starting level for upconversion.

The data presented in Fig. 11 do not allow a sensible estimation of E_q, the thermal quenching barrier. It can be seen that the levelling off of the radiance in Fig. 11 occurs at higher temperatures than in Fig. 10. This difference may be ascribed to the rather high value of E_u in type 2a curves as compared to E_u of type 1a, 1b and 1b.

Fig. 12 shows the temperature behaviour of the doublet at 532.2 nm. The two bands of this doublet show different temperature behaviour: band 532.1 nm shows the typical type 2a upconversion behaviour of $^4S_{3/2} \rightarrow {}^2H_{11/2}$ as shown in Fig. 11, whereas the 532.3 nm band shows type-2b behaviour. In Table 2 we have assigned the 532.3 nm band to the $^2P_{3/2} \rightarrow {}^4I_{9/2}$ transition. All peaks represented in Table 2 show this type 2b temperature behaviour. From the calculated value of E_u for the 532.1 nm transition we conclude that the upconversion is from the same $^4S_{3/2}$ sub-level ($M_J = \pm 3/2$)

3.4. Excitation energy

As mentioned in the previous section, we have recorded the LA-spectra of $Y_2O_3:Er^{3+}$ with a 10% and 25% transmission filter. If there are no saturation effects, it is to be expected that the spectral radiances of these spectra differ by a factor of 2.5. In Fig. 13 we have plotted the factor F, which is the radiance of a band measured with 25% filter divided by the radiance of that band at 10%, for various bands as a function of wavelength.

The dashed line at F = 2.5 indicates the expectation value for F. Only the two bands of the $^4F_{9/2} \rightarrow {}^4I_{15/2}$ multiplet (at 668.3 nm and 680.1 nm) show this expected value; the bands in the other multiplets yield higher F-values. In Fig. 6 it is shown that the $^4F_{9/2} \rightarrow {}^4I_{15/2}$ multiplet yields by far the strongest fluorescence in the LA-spectrum.

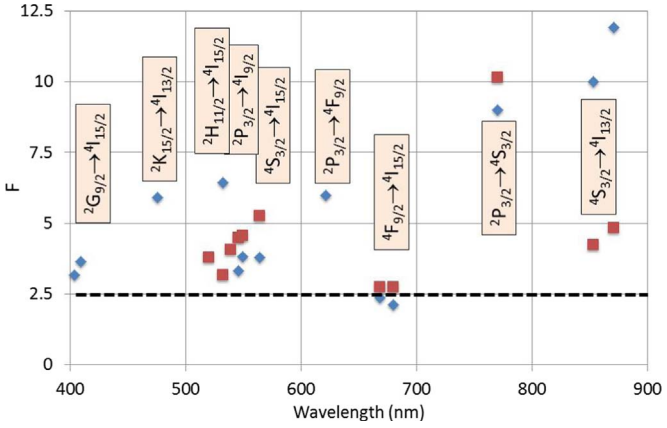

Fig. 13. Radiance ratio F of bands in LA-spectra of $Y_2O_3:Er^{3+}$ excited with 25% and 10% transmission filters. Blue diamonds: −190 °C, red squares: +30 °C. In various cases the radiance at +30 °C was too low to obtain a reliable figure for F. This was even the case at −190 °C for the very weak $^2H_{9/2} \rightarrow {}^4I_{9/2}$ bands.

Table 5
Level identification for hot band upconversion $^4S_{3/2} \rightarrow {}^2H_{11/2}$.

Band (nm)	$^2H_{11/2}$ level (cm^{-1}), Ref. [15]	E_u (cm^{-1})	Calculated $^4S_{3/2}$ level (cm^{-1})	$^4S_{3/2}$ level (cm^{-1}), Ref. [15]
519.7	19,244	820	18,424	18,318
539.3	19,045	650	18,395	18,318

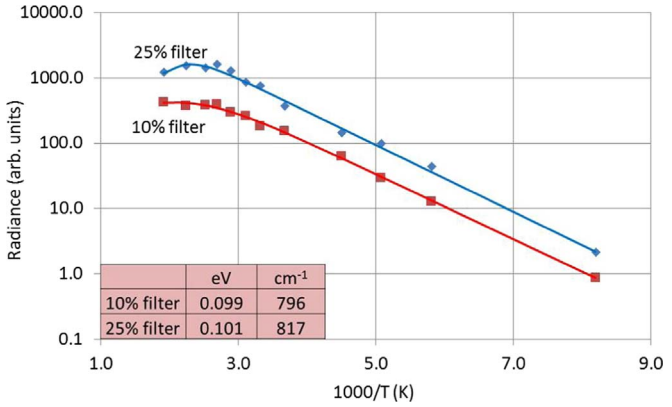

Fig. 14. Arrhenius plot of the radiance of the 519.7 nm band (belonging to the $^2H_{11/2} \rightarrow {}^4I_{15/2}$ multiplet) of $Y_2O_3:Er^{3+}$ at two different filter settings. The full curves are according to Eq. (4), fitted to the experimental points.

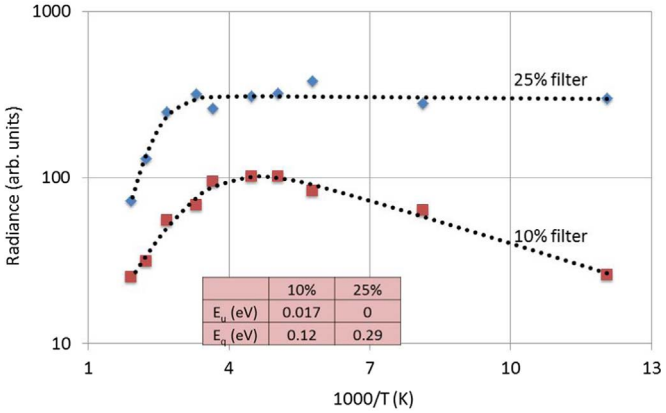

Fig. 15. Arrhenius plot of the radiance of the 871.2 nm band (belonging to the $^4S_{3/2} \rightarrow {}^4I_{13/2}$ multiplet) of $Y_2O_3:Er^{3+}$ at two different filter settings. The dotted curves are according to Eq. (4), fitted to the experimental points.

We may conclude that the total radiation energy is increased by a factor of 2.5 by changing the 10% filter for a 25% filter; moreover, it can also be concluded that there is no saturation at excitation using the 25% filter. All multiplets with F > 2.5 are involved in a two-photon absorption process, only the $^4F_{9/2} \rightarrow {}^4I_{15/2}$ multiplet refers to a one-photon excitation process. In other words, we may conclude that the two-photon absorption process for the other multiplets gets more efficient when the excitation energy is increased. However, the differences between the various multiplets suggest that there is additional reshuffling of the energy transfer by increasing the excitation energy.

Tanner and Wong [10] concluded from an analysis of the LA-spectrum of $Y_2O_3:Er^{3+}$ that the temperature in nanocrystalline material is higher than in bulk material as investigated by Kisliuk et al. [12]. If temperature effects play a role upon exciting nanocrystalline $Y_2O_3:Er^{3+}$ particles, then it is to be expected that the temperature upon excitation with a 25% filter increases more than upon exciting with the 10% filter. In Fig. 14, which is an Arrhenius plot of the temperature behaviour of the radiance of the 519.7 nm band for two filter settings, this hypothesis is tested for the LA-spectra presented in this report.

The slopes of the straight lines in Fig. 14 are equal taking the experimental spread of about ± 5% into account, while the levelling off takes place at the same temperature. Thus, the temperatures of the $Y_2O_3:Er^{3+}$ particles are equal at both filter settings: in fact we may conclude that there is no temperature increase upon irradiation with the laser.

Fig. 13 illustrates that the deviation from F = 2.5 is particularly large for the 853.1 nm and 871.2 nm bands of the $^4S_{3/2} \rightarrow {}^4I_{13/2}$ multiplet. For that reason we have analysed the temperature behaviour of the 871.1 nm band in more detail. The result is shown in Fig. 15, which is an Arrhenius plot of the radiance of the 871.2 nm band for two filter settings. Fig. 15 indicates a significant difference between the two filter settings: the 10% filter shows type 1c temperature behaviour, whereas the 25% filter has type 1b. The activation energy found for the type 1c behaviour of the 10% filter setting is 0.017 eV (137 cm^{-1}). The difference between the two settings shown in Fig. 15 will be considered in the next section.

4. Discussion

In this section we shall consider the various types of temperature behaviour as illustrated in Fig. 3. We shall make use of a conventional three-level scheme as shown in Fig. 16. In Fig. 16 we have presented two transitions from the $^4S_{3/2}$ energy level: for band 549.5 nm to the second highest sub-level of $^4I_{15/2}$ at the left-hand side and for band 871.1 nm to the second lowest sub-level of $^4I_{13/2}$ at the right-hand side. The difference between these two schemes is that the transition at the left-hand side shows type 1a temperature behaviour, whereas the right-hand band shows type 1b/1c character. It can be seen that for the type 1a transition the transition is from the M_J = 1/2 sub-level at 18,231 cm^{-1}, whereas for the other it is from the M_J = 3/2 sub-level at 18,318 cm^{-1}. It is assumed that the lowest level of $^4S_{3/2}$ gets populated during irradiation with the laser, indicated by the red arrows. This is largely through radiationless processes as indicated in Fig. 7 of Ref. [1]. Upon increasing the temperature the M_J = ± 3/2 sub-level gets gradually populated by vibronic effects with the consequence that the M_J = ± 1/2 level gets more depopulated. This explains the decrease of radiance of type-1a transitions in the low temperature region. The energy difference E_u between the two $^4S_{3/2}$ levels is 89 cm^{-1}, which is larger than we have calculated from the Arrhenius plot for the 549.5 nm band (70 cm^{-1}). However, in view of the rather large spread of the data points in Fig. 10, we consider this a fair agreement. In fact it is questionable whether it is realistic to represent the low temperature behaviour of the 1a and 1b types by a single activation energy E_u. The relatively large radiance at −190 °C for most 1a type bands causes a deviation from a straight line in the low temperature range as indicated in Fig. 3.

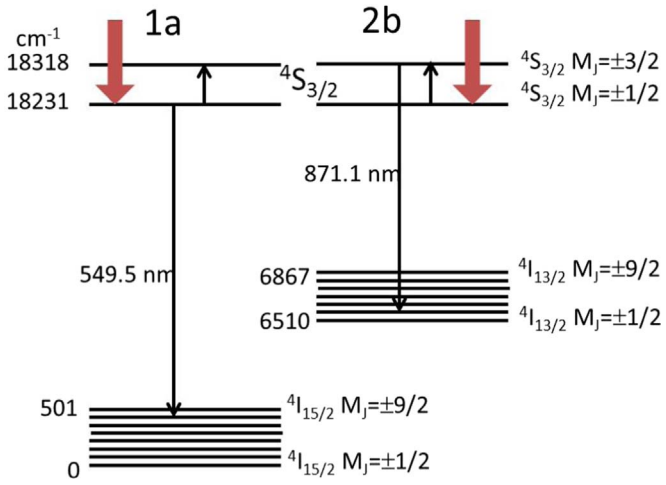

Fig. 16. Three-level scheme for $^4S_{3/2} \rightarrow {}^4I_{15/2}$ (left-hand side) and $^4S_{3/2} \rightarrow {}^4I_{13/2}$ (right-hand side) transitions of Er^{3+} in Y_2O_3. Only the energy of the top and bottom sub-levels of $^4I_{15/2}$ and $^4I_{13/2}$ has been indicated.

By the same reasoning it is to be expected that the right-hand scheme leads to hot-band characteristics, because the $^4S_{3/2}$ top level gets more populated upon increasing the temperature. That is indeed what we found in practice; however, the value found for E_u (137 cm^{-1}) from the Arrhenius type analysis shown in Fig. 15 for the 10% filter is larger than the energy difference (89 cm^{-1}) between the M_J = ± 3/2

and $M_J = \pm 1/2$ sub-levels of $^4S_{3/2}$. When the material is more strongly excited with the 25% transmission filter, it is assumed that the $^4S_{3/2}$ $M_J = 3/2$ level is also directly populated by laser energy. Vibronic upconversion is thus less important and we get the flat type 1b temperature behaviour shown in Fig. 15.

The 545.9 nm band, which has been analysed in Fig. 10, also starts from the $M_J = \pm 3/2$ sub-level of $^4S_{3/2}$ and is according to the reasoning above also expected to show type 1c character. The estimated low value of E_u deviates clearly from 89 cm^{-1}, which would be the expected value. We conclude from the above considerations that the three-level scheme in Fig. 16 explains the types 1a, 1b and 1c qualitatively, but that the quantitative explanation of the calculated values of E_u is still incomplete.

In the previous section we have already described the hot-band character of the type 2a behaviour of the $^2H_{11/2} \rightarrow {}^4I_{15/2}$ hot bands by upconversion from $^4S_{3/2}$ to $^2I_{11/2}$ in terms of a three-level scheme. Therefore, we shall finalize this discussion by considering the deviating behaviour of type 2b. We have observed this behaviour only in the five $^2P_{3/2} \rightarrow {}^4I_{9/2}$ bands that are shown in the spectrum recorded at −190 °C of Fig. 9. We shall present here an explanation in terms of a cross-relaxation process.

Fig. 17 is the cross-relaxation scheme for the reaction:

$$^2H_{11/2} + {}^4I_{9/2} \rightarrow {}^2P_{3/2} + {}^4I_{15/2} \quad (7)$$

At low temperatures, −190 °C < T < −100 °C, the 532.3 nm band (right-hand side of Fig. 17) shows type 1a temperature behaviour due to the fact that the $^2P_{3/2}$ $M_J = 1/2$ sub-level gets slightly depopulated by vibronic uplifting to the $M_J = 3/2$ sub-level when the temperature is increased by 100–125 °C. In the meanwhile the $^2H_{11/2}$ levels get populated as discussed in relation to Fig. 10: the 532.1 nm band shows type 2a behaviour. When the population density of the $^2H_{11/2}$ levels is sufficiently high, the cross relaxation indicated by the red arrows in Fig. 17 can take place. This means that the depopulation of the $^2P_{3/2}$ level stops and the temperature behaviour changes from type 1a to type 2a upon increasing the temperature.

The Dieke diagrams [21] and Gruber's et al. [15] data show the abundance of electronic levels of Er^{3+} in the near UV, visible and near IR. This makes it plausible that more cross-relaxation mechanisms may exist in Er^{3+}-doped phosphors. Liu [22] has mentioned the following additional cross-relaxations:

$$^4I_{11/2} + {}^2H_{11/2} \rightarrow {}^4I_{13/2} + {}^4F_{3/2} \quad (8a)$$

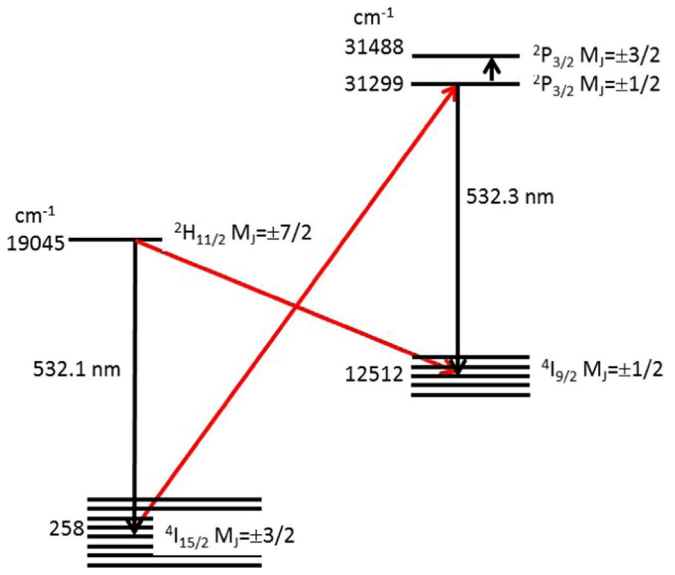

Fig. 17. Cross relaxation between $^2H_{11/2}$, $^4I_{9/2}$, $^2P_{3/2}$ and $^4I_{15/2}$. Energy levels have been taken from Gruber et al. [15].

$$^4F_{7/2} + {}^2H_{11/2} \rightarrow {}^2G_{9/2} + {}^4F_{9/2} \quad (8b)$$

If cross-relaxation (8b) would occur in the LA-spectra of $Y_2O_3:Er^{3+}$, it would be expected that the 409 nm band would (slightly) grow in intensity at temperatures > −50 °C. The low intensity of the bands in this spectral region does not allow us to make a conclusion on the occurrence of this cross-relaxation in the LA-spectra presented here.

In Fig. 4b it is shown that the FWHM of the 535 nm band makes a jump upon changing the temperature. Due to the cross-relaxation the electron-phonon interaction coefficient, α, as defined by Walsh and Di Bartolo [23], changes and this explains the FWHM-jump in Fig. 4b. It should be mentioned that the spread in the FWHM-data presented in Fig. 4 does not allow the evaluation of the phonon parameters T_D (the Debye temperature) and α_i for transition i. The cross-relaxation represented in Fig. 17 involves two different Er^{3+} ions, which must be sufficiently close in sustaining this process. From this inference it follows that at low Er^{3+} concentrations in Y_2O_3 the $^2P_{3/2} \rightarrow {}^4I_{9/2}$ transitions will show predominantly type 1a temperature behaviour. This will be the subject of a forthcoming investigation.

5. Conclusions

The most important result of the present study is the re-assignment of the electronic multiplets in the very rich and complicated LA-spectrum of cubic $Y_2O_3:Er^{3+}$. This re-assignment has been based on the recently published C_2-type Stark levels of $Y_2O_3:Er^{3+}$ by Gruber et al. [15]. Apart from very few peaks (only 6), the frequencies of all other peaks agreed within 6 cm^{-1} with the values calculated from Gruber´s data. We have categorised the temperature behaviour of the bands in an Arrhenius plot using a phenomenological equation, which is in fact a modified Fermi-Dirac equation. With this equation the activation energies of the $^2H_{11/2} \rightarrow {}^4I_{15/2}$ hot bands were calculated from the radiance of individual spectral transitions. The obtained upconversion activation energy of these hot bands enabled a tracing back to the original $^4S_{3/2}$ levels. Some of the spectral bands in the $^2H_{11/2} \rightarrow {}^4I_{15/2}$ multiplet region do not belong to this multiplet, but rather to the much weaker $^2P_{3/2} \rightarrow {}^4I_{9/2}$ multiplet. These latter bands have more complex temperature behaviour, which changes from type 1a at the lowest temperatures to 2a (hot hand character) at slightly higher temperatures. This odd temperature behaviour has been explained in terms of a cross-relaxation process that becomes more important when the population density of the $^2H_{11/2}$ levels gets larger upon increasing the temperature. The temperature behaviour of the 1a/1b/1c types cannot be described quantitatively, but we have explained this behaviour qualitatively in terms of down conversion and upconversion to neighbouring Kramers doublet levels. We have the intention to study the non-identified spectral bands and the $^2P_{3/2} \rightarrow {}^4I_{9/2}$ multiplet in the LA-spectrum of $Y_2O_3:Er^{3+}$ at different doping levels of Er^{3+} in the near future.

The further understanding of the behaviour of the hot bands in $Y_2O_3:Er^{3+}$ could be used in designing upconverting nanoparticles for in vivo and in vitro experiments. In the last few years there have been studies on upconversion phosphors to potentially form treatments to eliminate cancers using infrared lasers to pass energy through tissues from outside the body, monitoring hot bands may be a way of assessing localised body temperatures to avoid “cooking” or damaging other tissue near the growths [24].

Acknowledgments

We are grateful to the EPSRC and Technology Strategy Board (TSB) for funding the PURPOSE (TP11/MFE/6/1/AA129F; EP-SRC TS/G000271/1) and CONVERTED (JeS no. TS/1003053/1), PRISM (EP/N508974/1) and FAB3D programs. We are finally grateful to the TSB for funding the CONVERT program.

References

[1] J. Silver, M.I. Martinez-Rubio, T.G. Ireland, G.R. Fern, R. Withnall, The effect of particle morphology and crystallite size on the upconversion luminescence properties of erbium and ytterbium co-doped yttrium oxide phosphors, J. Phys. Chem. B 105 (2001) 948–953.

[2] D. Bera, L. Quan, P.H. Holloway, Phosphor quantum dots, in: A. Kitai (Ed.), Ch. 2 Luminescent Materials and Applications, J. Wiley, Chichester, 2008, pp. 19–73.

[3] J. Silver, R. Withnall, Color conversion phosphors for LEDS, in: A. Kitai (Ed.), Ch. 3 Luminescent Materials and applications, J. Wiley, Chichester, 2008, pp. 75–109.

[4] G. Yi, H. Lu, S. Zhao, Y. Ge, W. Yang, D. Chen, L.H. Guo, Synthesis, characterization, and biological application of size-controlled nanocrystalline $NaYF_4$:Yb,Er infrared-to-visible up-conversion phosphors, Nano Lett. 4 (2004) 2191–2196.

[5] A. Gnach, T. Lipinski, A. Bednarkiewicz, J. Rybkaab, J.A. Capobianco, Upconverting nanoparticles: assessing the toxicity, Chem. Soc. Rev. 44 (2015) 1561–1584.

[6] X. He, K. Wang, Z. Cheng, *In vivo* near-infrared fluorescence imaging of cancer with nanoparticle-based probes, Nanomed. Nanobiotechnol. 2 (2010) 349–366.

[7] M. Haase, H. Schäfer, Upconverting nanoparticles, Angew. Chem. Int. Ed. 50 (2011) 5808–5829.

[8] J. Silver, M.I. Martinez-Rubio, T.G. Ireland, G.R. Fern, R. Withnall, Yttrium oxide upconverting phosphors. Part 2: temperature dependent upconversion luminescence properties of erbium in yttrium oxide, J. Phys. Chem. B 105 (2001) 7200–7204.

[9] P.A. Tanner, X. Zhou, F. Liu, Assignment of electronic transitions and electron-phonon coupling of Er^{3+} doped into Y_2O_3, J. Phys. Chem. A 108 (2004) 11521–11525.

[10] P.A. Tanner, K.L. Wong, Synthesis and spectroscopy of lanthanide ion-doped Y_2O_3, J. Phys. Chem. B 108 (2004) 136–142.

[11] M.D. Shinn, W.A. Sibley, M.G. Drexhage, R.N. Brown, Optical transitions of Er+ ions in fluorozirconate glass, Phys. Rev. B 27 (1983) 6635–6648.

[12] P. Kisliuk, W.F. Krupke, J.B. Gruber, Spectrum of Er^{3+} in single crystals of Y_2O_3, J. Chem. Phys. 40 (1964) 3606–3610.

[13] N.C. Chang, J.B. Gruber, R.P. Leavitt, C.A. Morrison, Optical spectra, energy levels, and crystal-field analysis of tripositive rare earth ions in Y_2O_3. I. Kramers ions in C_2 sites, J. Chem. Phys. 76 (1982) 3877–3889.

[14] J.B. Gruber, K.L. Nash, D.K. Sardar, U.V. Valiev, N. Ter-Gabielyan, L.D. Merkle, Modeling optical transitions of Er^{3+} ($4f^{11}$) in C_2 and C_{3i} sites in polycrystalline Y_2O_3, J. Appl. Phys. 104 (2008) 023101.

[15] J.B. Gruber, G.W. Burdick, S. Chandra, D.K. Sardar, Analyses of the ultraviolet spectra of Er^{3+} in Er_2O_3 and Er^{3+} in Y_2O_3, J. Appl. Phys. 108 (2010) 023109.

[16] F. Baur, F. Glocker, T. Jüstel, Photoluminescence and energy transfer rates and efficiencies in Eu^{3+} activated $Tb_2Mo_3O_{12}$, J. Mater. Chem. C 3 (2015) 2054–2064.

[17] J. Ueda, P. Dorenbos, A.J.J. Bos, A. Meijerink, S. Tanabe, Insight into the thermal quenching mechanism for $Y_3Al_5O_{12}$:Ce^{3+} through thermo luminescence excitation spectroscopy, J. Phys. Chem. C 119 (2015) 25003–25008.

[18] X. Jing, T. Ireland, C. Gibbons, D.J. Barber, J. Silver, A. Vecht, G. Fern, P. Trogwa, D.C. Morton, Control of Y2O3:Eu spherical particle phosphor size, assembly properties, and performance for FED and HDTV, J. Electrochem. Soc. 146 (1999) 4654–4658.

[19] D. den Engelsen, P. Harris, T. Ireland, J. Silver, Cathodoluminescence of double layers of phosphor particles, ECS J. Solid State Sci. Technol. 3 (2014) R53–R59.

[20] A.N. Gruzintsev, Yu.V. Ermolaeva, N.A. Matveevskaya, A.S. Bezkrovnyi, A.V. Tolmachev, G.A. Emel'chenko, Size dependent luminescence of spherical Y_2O_3:Er nanoparticles, Inorg. Mater. 50 (2014) 1099–1103.

[21] G.H. Dieke, Spectra and Energy Levels of Rare Earth Ions in Crystals, Interscience, New York, London, 1968.

[22] G. Liu, Advances in the theoretical understanding of photon upconversion in rare-earth activated nanophosphors, Chem. Soc. Rev. 44 (2015) 1635–1652.

[23] B.M. Walsh, B. Di Bartolo, On the analysis of the thermal line shift and thermal line width of ions in solids, J. Lumin. 158 (2015) 265–267.

[24] G. Tian, X. Zhang, Z. Gu, Y. Zhao, Recent advances in upconversion nanoparticles-based multifunctional nanocomposites for combined cancer therapy, Adv. Mater. 27 (2015) 7692–7712.